Am J Cancer Res 2024;14(8):3826-3841
www.ajcr.us /ISSN:2156-6976/ajcr0158000

Original Article

Predictive machine learning models based on VASARI features for WHO grading, isocitrate dehydrogenase mutation, and 1p19q co-deletion status: a multicenter study

Wei Zhao[1], Chao Xie[2], Kukun Hanjiaerbieke[1], Rui Xu[1], Tuxunjiang Pahati[1], Shaoyu Wang[3], Junjie Li[4], Yunling Wang[1]

[1]Imaging Centre, The First Affiliated Hospital of Xinjiang Medical University, Urumqi 830054, Xinjiang, China; [2]Imaging Centre, The Seventh Affiliated Hospital of Xinjiang Medical University, Urumqi 832000, Xinjiang, China; [3]MR Research Collaboration, Siemens Healthineers, Beijing 100102, China; [4]Department of Radiology, Beijing Tiantan Hospital, Capital Medical University, Beijing 100070, China

Received May 23, 2024; Accepted August 8, 2024; Epub August 25, 2024; Published August 30, 2024

Abstract: The objective of our study was to develop predictive models using Visually Accessible Rembrandt Images (VASARI) magnetic resonance imaging (MRI) features combined with machine learning techniques to predict the World Health Organization (WHO) grade, isocitrate dehydrogenase (IDH) mutation status, and 1p19q co-deletion status of high-grade gliomas. To achieve this, we retrospectively included 485 patients with high-grade glioma from the First Affiliated Hospital of Xinjiang Medical University, of which 312 patients were randomly divided into a training set (n=218) and a test set (n=94) in a 7:3 ratio. Twenty-five VASARI MRI features were selected from an initial set of 30, and three machine learning models - Multilayer Perceptron (MP), Bernoulli Naive Bayes (BNB), and Logistic Regression (LR) - were trained using the training set. The most informative features were identified using recursive feature elimination. Model performance was assessed using the test set and an independent validation set of 173 patients from Beijing Tiantan Hospital. The results indicated that the MP model exhibited the highest predictive accuracy on the training set, achieving an area under the curve (AUC) close to 1, indicating perfect discrimination. However, its performance decreased in the test and validation sets; particularly for predicting the 1p19q co-deletion status, the AUC was only 0.703, suggesting potential overfitting. On the other hand, the BNB model demonstrated robust generalization on the test and validation sets, with AUC values of 0.8292 and 0.8106, respectively, for predicting IDH mutation status and 1p19q co-deletion status, indicating high accuracy, sensitivity, and specificity. The LR model also showed good performance with AUCs of 0.7845 and 0.8674 on the test and validation sets, respectively, for predicting IDH mutation status, although it was slightly inferior to the BNB model for the 1p19q co-deletion status. In conclusion, integrating VASARI MRI features with machine learning techniques shows promise for the non-invasive prediction of glioma molecular markers, which could guide treatment strategies and improve prognosis in glioma patients. Nonetheless, further model optimization and validation are necessary to enhance its clinical utility.

Keywords: Machine learning, visually accessible rembrandt images, glioma, isocitrate dehydrogenase mutation, 1p19q co-deletion

Introduction

Gliomas, a type of central nervous system (CNS) tumor, present a significant health challenge due to their aggressive nature and poor prognosis. Originating from glial cells that support and protect neurons in the brain and spinal cord, gliomas vary in type, including astrocytomas, oligodendrogliomas, and ependymomas, each differing in prognosis and treatment strategies [1]. Precise diagnosis, grading, and molecular profiling are essential for optimizing treatment approaches and enhancing patient outcomes [2, 3].

The World Health Organization CNS Tumor Classification 2021 (WHO CNS 2021) provides updated criteria for diagnosing and grading gliomas, highlighting the role of molecular markers in guiding prognosis and treatment decisions

https://doi.org/10.62347/MZLF2460

[4]. Magnetic resonance imaging (MRI), with its superior soft tissue resolution, offers detailed views of tumor characteristics through multi-sequence, multi-parametric, and multi-planar imaging. This capability is particularly valuable for glioma diagnosis, establishing MRI as an indispensable tool in glioma diagnostics, often reliant on conventional MRI sequences.

The Visually Accessible Rembrandt Images (VASARI) feature set is a standardized collection of radiological features tailored for MRI-based glioma assessment, aiding in enhancing diagnostic and prognostic accuracy [5]. VASARI features include a variety of morphological, contrast-enhanced, and diffusion characteristics, quantifying and enabling comparisons of tumor heterogeneity and biological behavior [6, 7]. These features capture aspects such as tumor location, enhancement pattern, necrosis, edema, and diffusion characteristics. Integrating VASARI features with WHO CNS 2021 criteria could advance the prediction of critical glioma molecular markers, such as isocitric dehydrogenase (IDH) mutation status and 1p19q co-deletion status, vital for personalized treatment planning and prognosis [8].

This study aims to use preoperative MRI-derived VASARI features to predict the WHO grade, IDH mutation status, and 1p19q co-deletion status of high-grade gliomas. To refine the predictive accuracy and clinical relevance of VASARI features, we have developed three machine learning models. These models were trained and evaluated using data from the First Affiliated Hospital of Xinjiang Medical University and independently validated using an external dataset from Beijing Tiantan Hospital, serving as an independent test set.

By leveraging VASARI MRI features and machine learning, our study aims to provide more precise and personalized predictions of glioma molecular markers. This methodology promises to enhance clinical decision-making, including treatment planning and prognosis evaluation, for glioma patients.

Materials and methods

Patients

This study received approval from the Ethics Committee of the First Affiliated Hospital of Xinjiang Medical University and adhered to the principles of the Declaration of Helsinki. As all data were anonymized, the committee waived the requirement for informed consent. All participants had been diagnosed with grade 3-4 CNS tumors per the 2021 World Health Organization (WHO) CNS tumor classification, and had complete clinical and pathological data available [4, 9]. The study period spanned from March 2018 to March 2024, during which 312 patients were enrolled at the First Affiliated Hospital of Xinjiang Medical University, and 173 patients at Beijing Tiantan Hospital.

Inclusion criteria: (1) Age 18 years or older. (2) Availability of complete pathological and immunohistochemical data, including WHO grade, IDH mutation status, and 1p19q co-deletion. (3) Diagnosis of grade 3-4 CNS tumors according to the 2021 WHO CNS tumor classification [4, 9].

Exclusion criteria: (1) Missing any required pathological data (WHO grade, IDH mutation status, or 1p19q co-deletion). (2) Incomplete preoperative MRI scans, specifically missing Diffusion Weighted Imaging (DWI) and Apparent Diffusion Coefficient (ADC) images. (3) MRI scans of poor quality with significant artifacts.

A project flowchart is presented in **Figure 1**.

MRI protocol

MRI scans were performed using a 3.0 Tesla scanner. The imaging protocol included axial T1-weighted images (T1WI), T1 contrast-enhanced (T1CE), T2-weighted images (T2WI), T2 Fluid Attenuated Inversion Recovery (T2FLAIR), DWI sequences (b-value =1000), and ADC maps. The contrast agent, dosed at 0.2 mmol/kg, was administered intravenously according to the patient's body weight. Detailed parameters of the MRI scanning sequences are outlined in **Table 1**.

Histopathological and immunohistochemical analysis

All tissue samples were obtained from biopsy results or fresh surgical tissues and were preserved in paraffin-embedded blocks. Surgical pathological tissues from both institutions were diagnosed according to the 2021 WHO classification. Cases diagnosed prior to this classifica-

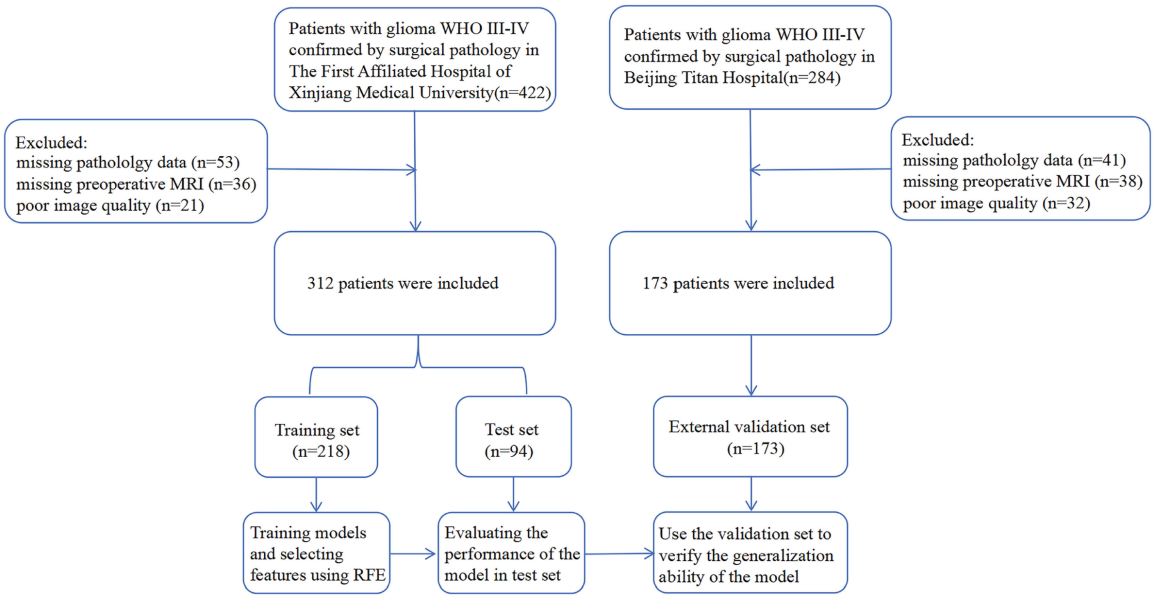

Figure 1. Research flowchart.

Table 1. MR scanning parameters in two institutions

Sequence		Philips ingenia CX 3.0T	GE Signa Architect 3.0T
T1WI	Scanning Sequence	GRE	FSE
	Time Echo	2 ms	24 ms
	Time repetition	6 ms	2016 ms
	Matrix	256×256	256×256
	Slice thickness	5 mm	6 mm
T2WI	Scanning Sequence	SE	FSE
	Time Echo	100 ms	102 ms
	Time repetition	2800 ms	3808 ms
	Matrix	256×256	256×256
	Slice thickness	5 mm	6 mm
T2-FLAIR	Scanning Sequence	IR	IR
	Time Echo	256 ms	126 ms
	Time repetition	4800 ms	7000 ms
	Matrix	256×256	256×256
	Slice thickness	5 mm	6 mm
DWI&ADC	Scanning Sequence	SE	EPI
	Time Echo	55 ms	min
	Time repetition	2000 ms	3110 ms
	Matrix	256×256	256×256
	Slice thickness	5 mm	6 mm
	b-value	0/1000	0/1000

MR: Magnetic Resonance, T1WI: T1-weighted images, T2WI: T2-weighted images, T2FLAIR: T2 Fluid Attenuated Inversion Recovery, DWI: Diffusion Weighted Imaging, ADC: Apparent Diffusion Coefficient.

tion were reclassified by senior pathologists (with over 20 years of experience) using the 2021 criteria.

The brain tumor tissues underwent a series of histopathological processes including fixation, embedding, sectioning, dewaxing, and dehy-

dration. The immunohistochemical protocol involved antigen retrieval, blocking non-specific binding sites, and the application of primary antibodies specific to mutant proteins. This was followed by detection using enzyme-labeled secondary antibodies, chromogenic reaction, counterstaining, and mounting. The presence of the IDH1 R132H mutation was determined by observing staining patterns (brown or red in the nucleus) under a microscope [10].

The Fluorescence In Situ Hybridization (FISH) method for 1p19q detection employed fluorescently labeled DNA probes to identify deletions in specific chromosomal segments. Tumor tissue samples, processed for fixation and sectioning, were treated to enhance chromosomal accessibility before applying probes targeting 1p and 19q regions, labeled with fluorescent dyes like Texas Red and FITC. After pretreatment, these sections underwent hybridization at controlled temperatures to facilitate probe binding. Post-hybridization, the slides were washed to remove unbound probes and impurities. The presence of 1p and 19q regions was assessed using a fluorescence microscope, where normal cells display two signal spots (one red, one green), and cells with deletions showed fewer or no spots. Technicians evaluated multiple cells to confirm 1p19q co-deletion, recording observations for statistical analysis [11].

VASARI features analysis

The VASARI feature set categorized gliomas into four distinct regions: (1) enhancing, (2) non-enhancing, (3) necrotic, and (4) edematous. A non-enhancing tumor is characterized by increased signal intensity on T2WI (lower than that of cerebrospinal fluid (CSF)) and decreased intensity on T1WI, often accompanied by mass effect and structural distortion, including blurring at the gray and white matter interface. Necrosis within tumors presents as areas without enhancement or with significantly reduced enhancement after contrast administration, appearing hyperintense on T2-weighted and proton density images, and hypointense on T1WI, bordered by irregular margins. Edema is identified by a signal intensity higher than that of non-contrast-enhancing tumors (nCET) yet slightly lower than that of CSF, with pseudopods as a distinguishing feature.

From the VASARI set of 30 features, 25 were selected for evaluation: F1, tumor location; F2, side of lesion center; F3, eloquent brain; F4, enhancement quality; F5, proportion enhancing; F6, proportion non-contrast-enhancing tumor; F7, proportion necrosis; F8, cysts; F9, multifocal or multicentric; F10, T1/FLAIR ratio; F11, thickness of enhancing margin; F12, definition of the enhancing margin; F13, definition of the non-enhancing margin; F14, proportion of edema; F15, edema crosses midline; F16, hemorrhage; F17, diffusion characteristics; F18, pial invasion; F19, ependymal invasion; F20, cortical involvement; F21, deep white matter invasion; F22, nonenhancing tumor crosses midline; F23, enhancing tumor crosses midline; F24, satellites; and F25, calvarial remodeling.

Two neuroimaging physicians, each with over ten years of experience, independently evaluated the brain MRI images using the VASARI features on a PACS workstation, blind to the pathological and immunohistochemical results. Discrepancies were resolved through consensus after discussion. Detailed descriptions of all features are available on the National Cancer Institute's Cancer Imaging Archive (https://wiki.cancerimagingarchive.net/display/Public/VASARI+Research+Project).

Feature selection and model development

We employed a recursive feature elimination (RFE) strategy alongside three machine learning models - Multilayer Perceptron (MP), Bernoulli Naive Bayes (BNB), and Logistic Regression (LR) - to isolate the most predictive features. Initially, patients from the First Affiliated Hospital of Xinjiang Medical University were randomly split into a training set (n=218) and a test set (n=94) using a 7:3 ratio. The training set facilitated both training and feature selection, whereas the test set assessed model performance. Through RFE, the feature set was iteratively refined by training and removing features until a predetermined threshold was met or further removal ceased to improve performance significantly. This process used the three models to evaluate and pinpoint the most critical features. Ultimately, a subset of features identified by RFE was utilized to build the final predictive model, which was then validat-

Table 2. Clinical characteristic data of all included patients

	First Affiliated Hospital of Xinjiang Medical University			X^2/t	p	Beijing Tiantan Hospital	X^2/t	p
	Training set (N=218)	Test set (N=94)	Total (N=312)			Validation set (N=173)		
Age (Years)	50.15±13.19	51.44±12.18	50.54±12.89	-0.81	0.418	50.90±11.94	0.303	0.762
Sex, n (%)				1.255	0.263		3.27	0.071
Female	94 (43.1%)	47 (50.0%)	141 (45.2%)			93 (53.8%)		
Male	124 (56.9%)	47 (50.0%)	171 (54.8%)			80 (46.2%)		
WHO Grade, n (%)				0.053	0.819		0.215	0.643
3	53 (24.3%)	24 (25.5%)	77 (24.7%)			46 (26.6%)		
4	165 (75.7%)	70 (74.5%)	235 (75.3%)			127 (73.4%)		
IDH status, n (%)				0.037	0.847		1.29	0.256
Wild-type	58 (26.6%)	26 (27.7%)	84 (26.9%)			118 (68.2%)		
Mutation	160 (73.4%)	68 (72.3%)	228 (73.1%)			55 (31.8%)		
1p19q co-deletion, n (%)				2.454	0.117		0.214	0.644
No	174 (79.8%)	82 (87.2%)	256 (82.1%)			139 (80.3%)		
Yes	44 (20.2%)	12 (12.8%)	56 (17.9%)			34 (19.7%)		

WHO: World Health Organization, IDH: isocitrate dehydrogenase.

ed using a test set and an external validation set from Beijing Tiantan Hospital (n=173). This integrated approach leveraged multiple models to effectively identify the most relevant features for accurate label prediction, thereby enhancing the model's generalizability.

Statistical analysis

Concordance between two observers was assessed using the Kappa test, where a Kappa score above 0.6 signifies substantial agreement. The interclass correlation coefficient (ICC) was used to measure the reliability of VASARI feature evaluation between observers, with an ICC greater than 0.75 indicating a high level of agreement. Categorical variables were analyzed using the chi-square test or Fisher's exact test as appropriate. The one-sample Kolmogorov-Smirnov test was employed to check for normality, and Levene's test for homoscedasticity. Parametric data were analyzed with independent samples t-tests, while non-parametric data were handled with Mann-Whitney U tests if the normality criterion was not met. Model performance was quantified using receiver operating characteristic (ROC) curve analysis, specifically calculating the area under the ROC curve (AUC). Additional metrics such as accuracy, sensitivity, specificity, and 95% confidence intervals were determined at the optimal Yorden index value. All statistical analyses were performed using a two-sided significance level with $P<0.05$ indicating statistical significance, and computations were conducted in Python (version 3.11.7).

Results

Observer consistency test

In terms of inter-observer agreement, the kappa coefficients ranged from 0.814 to 0.931, indicating a high degree of consensus among different observers on all VASARI features.

Patients clinical characteristics

According to the inclusion and exclusion criteria, a total of 485 patients were enrolled in our study. Patients from the First Affiliated Hospital of Xinjiang Medical University were divided into a training set (n=218) and a test set (n=94) using a 7:3 ratio. Patients from Beijing Tiantan Hospital comprised the external validation set (n=173). Detailed clinical information is presented in **Table 2**. There were no statistically significant differences in age, gender, WHO classification, IDH mutation status, or 1p19q co-deletion status across the training, test, and validation sets ($P>0.05$).

Patient VASARI characteristics

Analysis of the VASARI features revealed statistically significant differences across various molecular and pathological classifications, as determined by chi-square tests. Detailed results are available in **Table 3**. Notably, features such as F1 Tumor Location, F3 Eloquent Brain, F4 Enhancement Quality, F5 Proportion Enhancing, F6 Proportion nCET, F7 Proportion Necrosis, F11 Thickness of Enhancing Margin,

Table 3. Differences in WHO grading, IDH status and 1p19q co-deletion status in the VASARI feature set in the training set

	IDH status		X^2	*p*	WHO Grade		X^2	*p*	1p19q co-deletion		X^2	*p*
	Mutation (N=58)	Wild-type (N=160)			3 (N=53)	4 (N=165)			No (N=174)	Yes (N=44)		
F1 Tumor Location			20.209	0.001**			10.762	0.056			16.394	0.006**
Brainstem	0 (0.0%)	13 (8.1%)			3 (5.7%)	10 (6.1%)			11 (6.3%)	2 (4.5%)		
Frontal	37 (63.8%)	55 (34.4%)			31 (58.5%)	61 (37.0%)			63 (36.2%)	29 (65.9%)		
Insular	0 (0.0%)	11 (6.9%)			0 (0.0%)	11 (6.7%)			11 (6.3%)	0 (0.0%)		
Occipital	1 (1.7%)	10 (6.2%)			1 (1.9%)	10 (6.1%)			11 (6.3%)	0 (0.0%)		
Parietal	7 (12.1%)	27 (16.9%)			8 (15.1%)	26 (15.8%)			27 (15.5%)	7 (15.9%)		
Temporal	13 (22.4%)	44 (27.5%)			10 (18.9%)	47 (28.5%)			51 (29.3%)	6 (13.6%)		
F2 Side of Lesion Center			1.348	0.51			2.156	0.34			0.309	0.857
Center	2 (3.4%)	11 (6.9%)			1 (1.9%)	12 (7.3%)			10 (5.7%)	3 (6.8%)		
Left	26 (44.8%)	77 (48.1%)			27 (50.9%)	76 (46.1%)			81 (46.6%)	22 (50.0%)		
Right	30 (51.7%)	72 (45.0%)			25 (47.2%)	77 (46.7%)			83 (47.7%)	19 (43.2%)		
F3 Eloquent Brain			13.157	0.011*			5.451	0.244			5.274	0.26
Moter	3 (5.2%)	23 (14.4%)			3 (5.7%)	23 (13.9%)			22 (12.6%)	4 (9.1%)		
None	28 (48.3%)	75 (46.9%)			28 (52.8%)	75 (45.5%)			79 (45.4%)	24 (54.5%)		
SpeechMotor	22 (37.9%)	30 (18.8%)			16 (30.2%)	36 (21.8%)			39 (22.4%)	13 (29.5%)		
SpeechReceptive	4 (6.9%)	29 (18.1%)			5 (9.4%)	28 (17.0%)			30 (17.2%)	3 (6.8%)		
Vision	1 (1.7%)	3 (1.9%)			1 (1.9%)	3 (1.8%)			4 (2.3%)	0 (0.0%)		
F4 Enhancement Quality			33.943	0.000**			47.516	0.000**			4.5	0.105
Marked	34 (58.6%)	147 (91.9%)			28 (52.8%)	153 (92.7%)			149 (85.6%)	32 (72.7%)		
Mild	18 (31.0%)	11 (6.9%)			18 (34.0%)	11 (6.7%)			19 (10.9%)	10 (22.7%)		
None	6 (10.3%)	2 (1.2%)			7 (13.2%)	1 (0.6%)			6 (3.4%)	2 (4.5%)		
F5 Proportion Enhancing			18.73	0.000**			40.364	0.000**			3.46	0.326
34-67%	14 (24.1%)	65 (40.6%)			10 (18.9%)	69 (41.8%)			64 (36.8%)	15 (34.1%)		
68-95%	2 (3.4%)	23 (14.4%)			1 (1.9%)	24 (14.5%)			23 (13.2%)	2 (4.5%)		
6-33%	28 (48.3%)	60 (37.5%)			24 (45.3%)	64 (38.8%)			68 (39.1%)	20 (45.5%)		
<5%	14 (24.1%)	12 (7.5%)			18 (34.0%)	8 (4.8%)			19 (10.9%)	7 (15.9%)		
F6 Proportion nCET			20.663	0.001**			40.929	0.000**			5.585	0.349
1	6 (10.3%)	2 (1.2%)			7 (13.2%)	1 (0.6%)			6 (3.4%)	2 (4.5%)		
34-67%	16 (27.6%)	65 (40.6%)			10 (18.9%)	71 (43.0%)			67 (38.5%)	14 (31.8%)		
68-95%	27 (46.6%)	58 (36.2%)			26 (49.1%)	59 (35.8%)			63 (36.2%)	22 (50.0%)		
6-33%	2 (3.4%)	22 (13.8%)			1 (1.9%)	23 (13.9%)			22 (12.6%)	2 (4.5%)		
<5%	0 (0.0%)	4 (2.5%)			0 (0.0%)	4 (2.4%)			4 (2.3%)	0 (0.0%)		
>95%	7 (12.1%)	9 (5.6%)			9 (17.0%)	7 (4.2%)			12 (6.9%)	4 (9.1%)		

F7 Proportion Necrosis			19.18	0.001**			25.069	0.000**			9.55	0.049*
34-67%	7 (12.1%)	41 (25.6%)			4 (7.5%)	44 (26.7%)			45 (25.9%)	3 (6.8%)		
68-95%	2 (3.4%)	3 (1.9%)			1 (1.9%)	4 (2.4%)			4 (2.3%)	1 (2.3%)		
6-33%	21 (36.2%)	84 (52.5%)			20 (37.7%)	85 (51.5%)			83 (47.7%)	22 (50.0%)		
None	6 (10.3%)	9 (5.6%)			6 (11.3%)	9 (5.5%)			11 (6.3%)	4 (9.1%)		
<5%	22 (37.9%)	23 (14.4%)			22 (41.5%)	23 (13.9%)			31 (17.8%)	14 (31.8%)		
F8 Cysts			0.167	0.683			0.258	0.612			0.565	0.452
No	20 (34.5%)	60 (37.5%)			21 (39.6%)	59 (35.8%)			66 (37.9%)	14 (31.8%)		
Yes	38 (65.5%)	100 (62.5%)			32 (60.4%)	106 (64.2%)			108 (62.1%)	30 (68.2%)		
F9 Multinfocal or Multicentric			2.507	0.474			9.595	0.022*			3.298	0.348
Gliomatosis	6 (10.3%)	10 (6.2%)			8 (15.1%)	8 (4.8%)			14 (8.0%)	2 (4.5%)		
Multicentric	2 (3.4%)	11 (6.9%)			1 (1.9%)	12 (7.3%)			12 (6.9%)	1 (2.3%)		
Multinfocal	12 (20.7%)	42 (26.2%)			9 (17.0%)	45 (27.3%)			45 (25.9%)	9 (20.5%)		
n/a	38 (65.5%)	97 (60.6%)			35 (66.0%)	100 (60.6%)			103 (59.2%)	32 (72.7%)		
F10 T1/FLAIR ratio			0.925	0.63			0.884	0.643			1.508	0.471
Expansive	28 (48.3%)	89 (55.6%)			26 (49.1%)	91 (55.2%)			97 (55.7%)	20 (45.5%)		
Infiltrative	11 (19.0%)	26 (16.2%)			11 (20.8%)	26 (15.8%)			28 (16.1%)	9 (20.5%)		
Mixed	19 (32.8%)	45 (28.1%)			16 (30.2%)	48 (29.1%)			49 (28.2%)	15 (34.1%)		
F11 Thickness of enhancing margin			13.44	0.001**			10.677	0.005**			5.782	0.056
Solid	8 (13.8%)	10 (6.2%)			6 (11.3%)	12 (7.3%)			11 (6.3%)	7 (15.9%)		
Thick/nodular (≥3 mm)	15 (25.9%)	85 (53.1%)			14 (26.4%)	86 (52.1%)			85 (48.9%)	15 (34.1%)		
Thin (<3 mm)	35 (60.3%)	65 (40.6%)			33 (62.3%)	67 (40.6%)			78 (44.8%)	22 (50.0%)		
F12 Definition of the enhancing margin			24.279	0.000**			31.253	0.000**			3.241	0.072
Poorly-defined	32 (55.2%)	33 (20.6%)			32 (60.4%)	33 (20.0%)			47 (27.0%)	18 (40.9%)		
Well-defined	26 (44.8%)	127 (79.4%)			21 (39.6%)	132 (80.0%)			127 (73.0%)	26 (59.1%)		
F13 Definition of the Non-Enhancing Margin			0.263	0.608			0.342	0.559			0.384	0.535
Poorly-defined	37 (63.8%)	108 (67.5%)			37 (69.8%)	108 (65.5%)			114 (65.5%)	31 (70.5%)		
Well-defined	21 (36.2%)	52 (32.5%)			16 (30.2%)	57 (34.5%)			60 (34.5%)	13 (29.5%)		
F14 Proportion of Edema			6.787	0.079			9.931	0.019*			3.908	0.272
34-67%	22 (37.9%)	84 (52.5%)			16 (30.2%)	90 (54.5%)			90 (51.7%)	16 (36.4%)		
6-33%	24 (41.4%)	60 (37.5%)			27 (50.9%)	57 (34.5%)			62 (35.6%)	22 (50.0%)		
None	2 (3.4%)	5 (3.1%)			3 (5.7%)	4 (2.4%)			6 (3.4%)	1 (2.3%)		
<5%	10 (17.2%)	11 (6.9%)			7 (13.2%)	14 (8.5%)			16 (9.2%)	5 (11.4%)		
F15 edema cross midline			0.029	0.865			0.047	0.829			3.358	0.067
No	47 (81.0%)	128 (80.0%)			42 (79.2%)	133 (80.6%)			144 (82.8%)	31 (70.5%)		
Yes	11 (19.0%)	32 (20.0%)			11 (20.8%)	32 (19.4%)			30 (17.2%)	13 (29.5%)		

F16 Hemorrhage			1.416	0.234			3.094	0.079			0.043	0.835
No	35 (60.3%)	82 (51.2%)			34 (64.2%)	83 (50.3%)			94 (54.0%)	23 (52.3%)		
Yes	23 (39.7%)	78 (48.8%)			19 (35.8%)	82 (49.7%)			80 (46.0%)	21 (47.7%)		
F17 Diffusion Characteristics			2.497	0.287			10.925	0.004**			0.235	0.889
Facilitated	19 (32.8%)	36 (22.5%)			21 (39.6%)	34 (20.6%)			43 (24.7%)	12 (27.3%)		
Mixed	17 (29.3%)	50 (31.2%)			18 (34.0%)	49 (29.7%)			53 (30.5%)	14 (31.8%)		
Restricted	22 (37.9%)	74 (46.2%)			14 (26.4%)	82 (49.7%)			78 (44.8%)	18 (40.9%)		
F18 Pial Invasion			1.256	0.262			1.193	0.275			2.125	0.145
No	31 (53.4%)	99 (61.9%)			35 (66.0%)	95 (57.6%)			108 (62.1%)	22 (50.0%)		
Yes	27 (46.6%)	61 (38.1%)			18 (34.0%)	70 (42.4%)			66 (37.9%)	22 (50.0%)		
F19 Ependymal Invasion			2.231	0.135			2.709	0.1			2.227	0.136
No	32 (55.2%)	70 (43.8%)			30 (56.6%)	72 (43.6%)			77 (44.3%)	25 (56.8%)		
Yes	26 (44.8%)	90 (56.2%)			23 (43.4%)	93 (56.4%)			97 (55.7%)	19 (43.2%)		
F20 Cortical Involvement			3.188	0.074			0.991	0.32			1.55	0.213
No	11 (19.0%)	50 (31.2%)			12 (22.6%)	49 (29.7%)			52 (29.9%)	9 (20.5%)		
Yes	47 (81.0%)	110 (68.8%)			41 (77.4%)	116 (70.3%)			122 (70.1%)	35 (79.5%)		
F21 Deep White Matter Invasion			7.238	0.007**			7.132	0.008**			4.67	0.031*
No	28 (48.3%)	46 (28.8%)			26 (49.1%)	48 (29.1%)			53 (30.5%)	21 (47.7%)		
Yes	30 (51.7%)	114 (71.2%)			27 (50.9%)	117 (70.9%)			121 (69.5%)	23 (52.3%)		
F22 Nonenhancing Tumor Crosses Midline			0.332	0.564			0.018	0.893			0.544	0.461
No	45 (77.6%)	118 (73.8%)			40 (75.5%)	123 (74.5%)			132 (75.9%)	31 (70.5%)		
Yes	13 (22.4%)	42 (26.2%)			13 (24.5%)	42 (25.5%)			42 (24.1%)	13 (29.5%)		
F23 Enhancing Tumor Crosses Midline			0.903	0.342			2.057	0.151			0.247	0.619
No	50 (86.2%)	129 (80.6%)			47 (88.7%)	132 (80.0%)			144 (82.8%)	35 (79.5%)		
Yes	8 (13.8%)	31 (19.4%)			6 (11.3%)	33 (20.0%)			30 (17.2%)	9 (20.5%)		
F24 Satellites			5.879	0.015*			3.843	0.050*			3.195	0.074
No	47 (81.0%)	102 (63.8%)			42 (79.2%)	107 (64.8%)			114 (65.5%)	35 (79.5%)		
Yes	11 (19.0%)	58 (36.2%)			11 (20.8%)	58 (35.2%)			60 (34.5%)	9 (20.5%)		
F25 Calvarial Remodeling			0.05	0.824			0.631	0.427			0.54	0.462
No	50 (86.2%)	136 (85.0%)			47 (88.7%)	139 (84.2%)			150 (86.2%)	36 (81.8%)		
Yes	8 (13.8%)	24 (15.0%)			6 (11.3%)	26 (15.8%)			24 (13.8%)	8 (18.2%)		

WHO: World Health Organization, IDH: isocitrate dehydrogenase, VASARI: Visually Accessible Rembrandt Images, nCET: non-contrast-enhancing tumors.

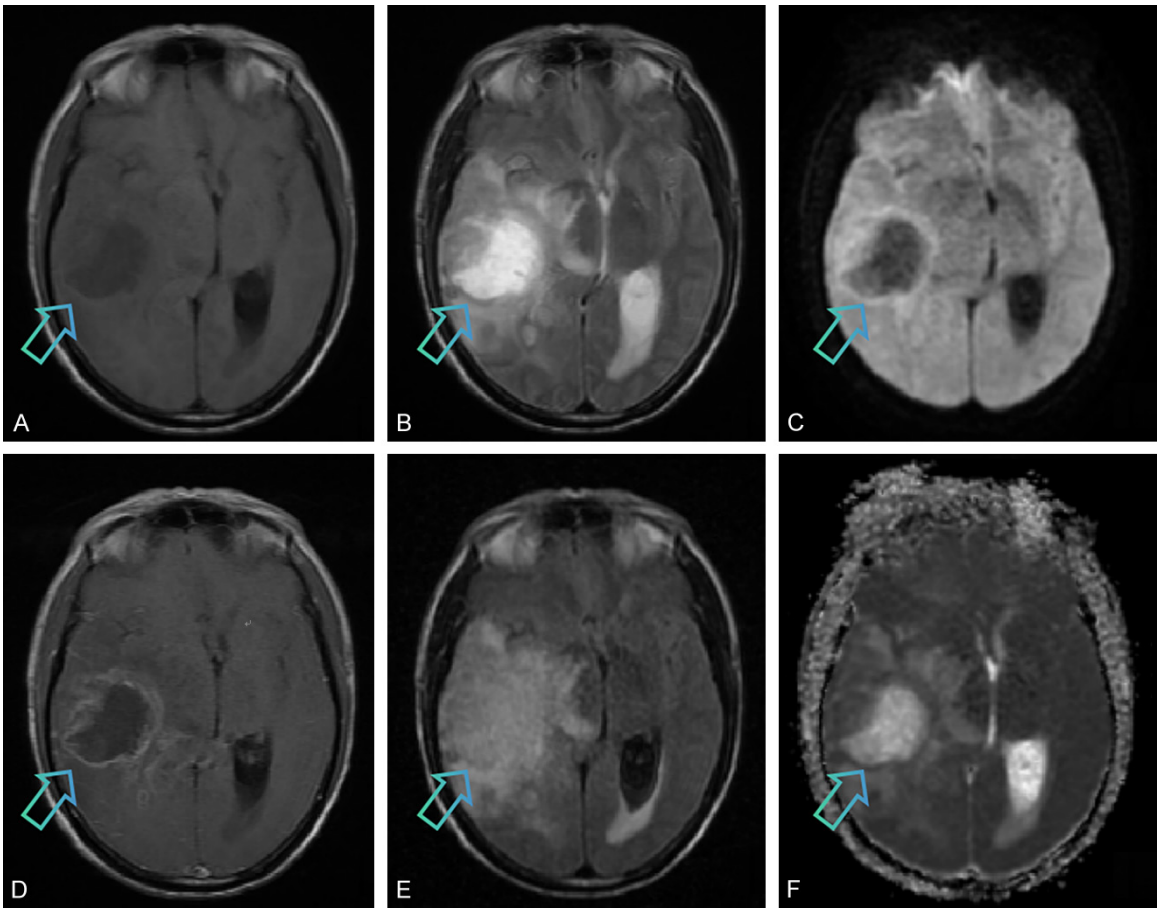

Figure 2. The patient was a 49-year-old male with WHO grade 4, IDH wild type, and 1p19q non-congruent deletion. The lesion is located in the right temporal lobe. A and B: Images showing hypointense at T1WI and hyperintense at T2WI; C: Slightly hyperintense at the FLAIR sequence, with peripheral patchy edema; D: Marked garland-like enhancement on CE-T1WI; E and F: Irregular hyperintense at the edge of the diffusion sequence, and hypointense in the center. The necrotic area is roughly 34%-67% with deep cerebral white matter invasion. WHO: World Health Organization, IDH: isocitrate dehydrogenase, T1WI: T1-weighted images, T2WI: T2-weighted images, FLAIR: Fluid Attenuated Inversion Recovery.

F12 Definition of Enhancing Margin, F21 Deep White Matter Invasion, and F24 Satellites showed significant associations with IDH status ($P<0.05$), suggesting their relevance in distinguishing between IDH wild-type and mutant types. For the WHO CNS grading, similar significant distinctions were observed for some of the aforementioned features between grades 3 and 4, highlighting their potential to differentiate glioma grades and provide prognostic insights.

Furthermore, the features of tumor location, proportion of necrosis, and deep white matter invasion demonstrated statistical significance in predicting 1p19q co-deletion status, indicating their utility in identifying this specific molecular characteristic of gliomas. The imaging characteristics of patients are depicted in **Figures 2** and **3**.

Predictive modeling and model evaluation

To develop a robust predictive model, we employed a RFE approach alongside three machine learning algorithms: MP, BNB, and LR. We trained these models using the training set from the First Affiliated Hospital of Xinjiang Medical University to identify the most informative features, then evaluated their performance using a test set, and further validated the results with an external dataset from Beijing Tiantan Hospital.

Tables 4-**6** provide a succinct summary of the model assessment outcomes, and **Figure 4**

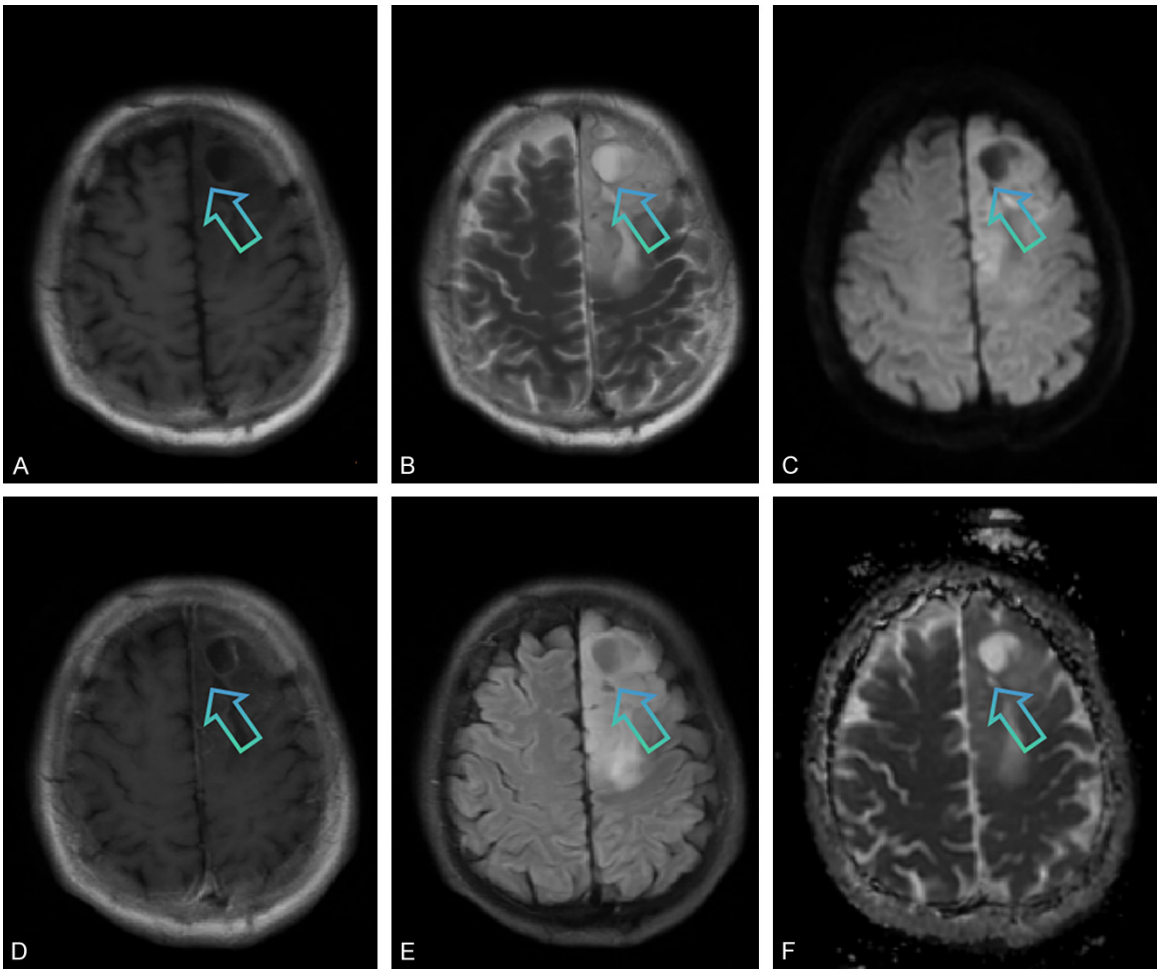

Figure 3. The patient is a 52-year-old male with a WHO grade 3 tumor, IDH mutation, and 1p19q co-deletion. The lesion is located in the left frontal lobe. A and B: Images showing slightly hypointense on T1-weighted images and slightly hyperintense on T2-weighted images; C: The FLAIR sequence shows slightly hyperintense signal; D: After contrast administration, the lesion exhibits abnormal enhancement with a sponge-like appearance; E and F: On the diffusion-weighted imaging, parts of the lesion show slightly hyperintense signal. The necrotic area is estimated to be about 6%-33%, and there is no invasion into the deep white matter. WHO: World Health Organization, IDH: isocitrate dehydrogenase, FLAIR: Fluid Attenuated Inversion Recovery.

illustrates the Receiver Operating Characteristic (ROC) curves and the Area Under the Curve (AUC). The MP model displayed superior prediction performance on the training set, with AUC values nearing 1, indicating perfect discrimination. However, the model's AUC decreased in the test and validation sets, particularly for predicting the 1p19q co-deletion state, with AUC values of 0.7612 and 0.703, suggesting potential overfitting issues. The BNB model demonstrated strong generalization capabilities, with AUC values of 0.8292 and 0.8106 for predicting IDH status, and 0.8982 and 0.9153 for the 1p19q co-deletion state, respectively, showcasing its accuracy, sensitivity, and specificity.

The LR model yielded AUCs of 0.7845 and 0.8674 on the test and validation sets, respectively, for IDH status prediction, and 0.7419 and 0.7896 for 1p19q co-deletion status, indicating effective but slightly inferior performance compared to the Bernoulli model in predicting 1p19q co-deletion status.

Our findings demonstrated that combining the RFE method with these machine learning models enables the successful identification and utilization of the most informative features to construct predictive models for gliomas' molecular and pathological characteristics. The models showed commendable generaliza-

Table 4. Performance of various machine learning models for predicting WHO class, IDH status, and 1p19q co-deletion on a training set

	Model	AUC	95% CI	F1_score	ACC	Sensitivity	Specifity
WHO Grade	MP	0.9999	[0.9998-1]	0.997	0.9954	1	0.9811
	BNB	0.8814	[0.8319-0.9308]	0.8955	0.8394	0.9091	0.6226
	LR	0.9183	[0.8802-0.9564]	0.8875	0.8394	0.8364	0.8491
IDH status	MP	1	[1-1]	1	1	1	1
	BNB	0.8621	[0.8052-0.919]	0.884	0.8303	0.8812	0.6897
	LR	0.9084	[0.8661-0.9507]	0.8771	0.8303	0.825	0.8448
1p19q codeletion	MP	1	[1-1]	1	1	1	1
	BNB	0.8106	[0.7444-0.8768]	0.5806	0.8211	0.6136	0.8736
	LR	0.8431	[0.7893-0.897]	0.5229	0.6651	0.9091	0.6034

WHO: World Health Organization, IDH: isocitrate dehydrogenase, MP: Multilayer Perceptron, BNB: Bernoulli Naive Bayes, LR: Logistic Regression.

Table 5. Performance of various machine learning models for predicting WHO class, IDH status, and 1p19q co-deletion on a test set

	Model	AUC	95% CI	F1_score	ACC	Sensitivity	Specifity
WHO Grade	MP	0.8304	[0.7381-0.9226]	0.8714	0.8085	0.8714	0.625
	BNB	0.8982	[0.8319-0.9308]	0.8955	0.8394	0.9091	0.6226
	LR	0.8637	[0.7801-0.9473]	0.8397	0.7766	0.7857	0.75
IDH status	MP	0.7885	[0.69-0.8869]	0.8227	0.734	0.8529	0.4231
	BNB	0.8292	[0.7396-0.9188]	0.8951	0.8404	0.9412	0.5769
	LR	0.7845	[0.6732-0.8958]	0.8182	0.7447	0.7941	0.6154
1p19q codeletion	MP	0.7612	[0.6259-0.8965]	0.4286	0.8298	0.5	0.878
	BNB	0.8465	[0.7504-0.9427]	0.4375	0.8085	0.5833	0.8415
	LR	0.7419	[0.6116-0.8721]	0.3235	0.5106	0.9167	0.4512

WHO: World Health Organization, IDH: isocitrate dehydrogenase, MP: Multilayer Perceptron, BNB: Bernoulli Naive Bayes, LR: Logistic Regression.

Table 6. Performance of various machine learning models for predicting WHO class, IDH status, and 1p19q co-deletion on a validation set

		AUC	95% CI	F1_score	ACC	Sensitivity	Specifity
WHO Grade	MP	0.8891	0.89 [0.8395-0.9386]	0.8745	0.8208	0.8504	0.7391
	BNB	0.9153	0.92 [0.8738-0.9567]	0.8945	0.8555	0.8346	0.913
	LR	0.9048	0.90 [0.8604-0.9492]	0.8546	0.8092	0.7638	0.9348
IDH status	MP	0.8585	0.86 [0.7954-0.9216]	0.8879	0.8497	0.8729	0.8
	BNB	0.9042	0.90 [0.8508-0.9576]	0.9004	0.8671	0.8814	0.8364
	LR	0.8674	0.87 [0.8049-0.93]	0.8507	0.8092	0.7966	0.8364
1p19q codeletion	MP	0.703	0.70 [0.6129-0.7932]	0.2951	0.7514	0.2647	0.8705
	BNB	0.8632	0.86 [0.7941-0.9323]	0.6173	0.8208	0.7353	0.8417
	LR	0.7896	0.79 [0.7062-0.8729]	0.4203	0.5376	0.8529	0.4604

WHO: World Health Organization, IDH: isocitrate dehydrogenase, MP: Multilayer Perceptron, BNB: Bernoulli Naive Bayes, LR: Logistic Regression.

tion across test and validation sets, offering a viable method for non-invasive prediction of glioma molecular markers using MRI imaging. Future work will focus on optimizing these models and expanding validation on additional datasets to enhance clinical applicability.

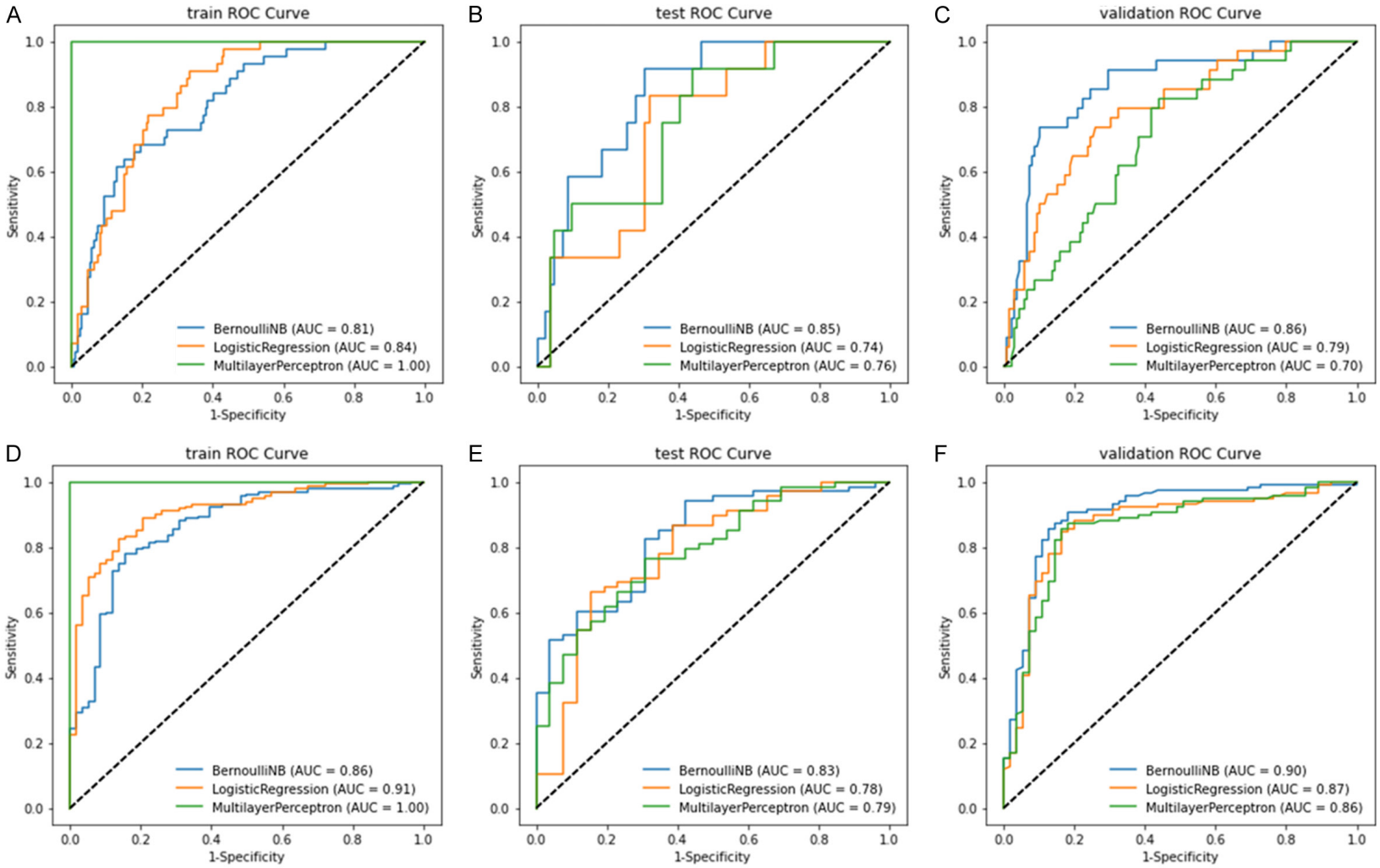
A
train ROC Curve
BernoulliNB (AUC = 0.81)
LogisticRegression (AUC = 0.84)
MultilayerPerceptron (AUC = 1.00)
B
test ROC Curve
BernoulliNB (AUC = 0.85)
LogisticRegression (AUC = 0.74)
MultilayerPerceptron (AUC = 0.76)
C
validation ROC Curve
BernoulliNB (AUC = 0.86)
LogisticRegression (AUC = 0.79)
MultilayerPerceptron (AUC = 0.70)
D
train ROC Curve
BernoulliNB (AUC = 0.86)
LogisticRegression (AUC = 0.91)
MultilayerPerceptron (AUC = 1.00)
E
test ROC Curve
BernoulliNB (AUC = 0.83)
LogisticRegression (AUC = 0.78)
MultilayerPerceptron (AUC = 0.79)
F
validation ROC Curve
BernoulliNB (AUC = 0.90)
LogisticRegression (AUC = 0.87)
MultilayerPerceptron (AUC = 0.86)
Sensitivity
1-Specificity

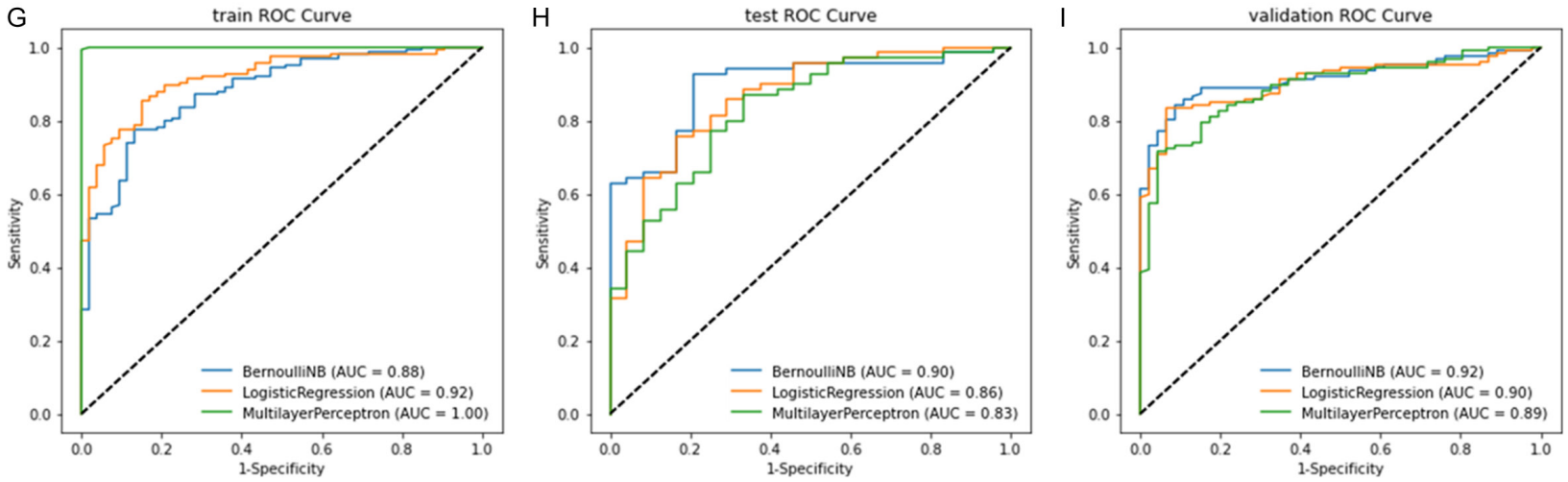

Figure 4. VASARI feature receiver operating characteristic curve (ROC) analysis of three machine learning models distinguishing 1p19q co-deletion status, IDH wild-type vs. mutant, and WHO grade 3 and 4. A: Area under the curve (AUC) of the three models in the training set to distinguish 1p19q co-deletion status; B: AUC of the three models in the test set to distinguish 1p19q co-deletion status; C: AUC of the three models in the validation set to distinguish 1p19q co-deletion status; D: AUC of the three models in the training set to distinguish IDH wild-type and mutant status; E: AUC of the three models in the test set to distinguish IDH wild-type and mutant status; F: AUC of the three models in the validation set to distinguish IDH wild-type and mutant status; G: AUC of the three models in the training set to distinguish WHO grade 3 and 4; H: AUC of the three models in the test set to distinguish WHO grade 3 and 4; I: AUC of the three models in the validation set to distinguish WHO grade 3 and 4. WHO: World Health Organization, IDH: isocitrate dehydrogenase, VASARI: Visually Accessible Rembrandt Images.

Discussion

Gliomas, the most prevalent primary malignant brain tumors, constitute over 80% of all primary brain tumors. Accurate identification and classification of gliomas are essential for guiding therapy and predicting prognosis. Recent advancements have emphasized the prognostic significance of molecular markers such as IDH mutation and 1p19q co-deletion status, which are increasingly utilized to tailor individual treatment strategies [12-15].

In this study, we utilized the VASARI MRI feature set to examine the imaging characteristics of gliomas and integrated it with machine learning techniques to develop predictive models for WHO grade, IDH mutation status, and 1p19q co-deletion status. In the training dataset, the MP model demonstrated optimal performance, achieving AUC values of 1 across all predictive metrics, indicative of exceptional predictive accuracy. However, its AUC values diminished in the validation and test datasets, notably for predicting the 1p19q co-deletion, where the AUC dropped to 0.703. This decrease suggests potential overfitting to the training data, resulting in lower accuracy in the validation and test datasets. Conversely, the BNB model exhibited robust predictive capability in these datasets, with AUC values consistently above 0.86. Particularly for WHO grade and IDH status, the AUC values reached 0.9153 and 0.9042, respectively, demonstrating the model's strong generalization ability. The LR model performed well in predicting IDH status in the validation dataset, achieving an AUC of 0.9084. However, its performance declined in the test dataset, especially in predicting 1p19q co-deletion, where the AUC was only 0.7419, indicating a reduced capacity to generalize its learned knowledge, particularly for 1p19q co-deletion.

Previous research [6-8] also underscores the predictive value of MRI features in gliomas. Prognosis was linked to certain morphological parameters such as tumor location, enhancement pattern, and extent of edema. Bai et al. [16] explored the predictive potential of preoperative Ki-67 proliferation index levels in IDH wild-type glioblastoma patients using VASARI MRI features. They identified the maximum diameter, proportion of necrosis, and presence of hemorrhage as independent predictors. Consistent with their findings, our study observed that the necrosis component in IDH wild-type glioma patients predominantly ranged between 6-33% and 34-67%, highlighting the clinical value of VASARI features in predicting preoperative Ki-67 proliferation index levels in this patient group.

Sacli-Bilmez et al. [17] utilized a supervised machine learning model that incorporated both clinical and VASARI MRI features to predict overall survival in glioblastoma patients. Their study highlighted that features like the proportion of non-enhancing components and necrosis were strongly correlated with survival, and that model performance improved with feature selection and oversampling. While our study did not focus on survival in high-grade glioma patients, the ratio of non-enhancing components to necrosis within the VASARI feature set proved effective in distinguishing WHO grade, IDH wild versus mutant status, and 1p19q co-deletion status. Their findings reinforce the efficacy of integrating clinical and VASARI features to differentiate glioblastoma patients with longer survival durations.

Verduin et al. [18] developed a prognostic model by combining clinical, VASARI, and additional radiological features to predict overall survival in patients with IDH wild-type glioblastoma, validated against an independent dataset. This underscores the potential of amalgamating clinical and imaging features in prognosis and molecular marker prediction in glioblastoma.

Studies have shown that low-grade gliomas with IDH mutations and 1p/19q deletions generally forecast a favorable prognosis and respond well to alkylating chemotherapy [19]. In Park's research [20], gliomas with concurrent IDH1 mutations and 1p/19q deletions typically exhibited a mixed pattern of high and intermediate ADC values or restricted diffusion properties, as well as increased instances of dural invasion, compared to gliomas with only IDH1 mutations. While there has been debate concerning the relationship between 1p/19q deletions and tumor boundaries, our findings indicated a correlation between 1p19q deletion status and factors such as tumor location, necrosis percentage, and deep white matter invasion. Further investigation in larger, more homogeneous populations are necessary to confirm these results.

The VASARI feature set, as a standardized radiological framework, provides comprehensive insights into glioma imaging characteristics [21-24]. Our analysis revealed significant variations in features like tumor location, enhancement quality, and proportion of necrosis among different molecular and pathological glioma subtypes, suggesting their utility in distinguishing these subtypes.

By employing machine learning techniques, we can refine VASARI MRI characteristics to isolate the most impactful features and develop precise predictive models. In this study, the RFE method was coupled with three machine learning algorithms: MP, BNB, and LR. The MP model excelled in the training set, whereas the BNB demonstrated robust generalization in the test and validation sets. These results affirm that RFE, combined with machine learning models, effectively selects pivotal features and constructs models with strong generalization capabilities.

The predictive models developed in this study are clinically valuable. Accurate predictions of WHO grade, IDH mutation status, and 1p19q co-deletion status can significantly guide treatment decisions and prognosis assessments in glioma patients. For instance, gliomas with IDH mutations generally have a favorable prognosis and respond well to chemotherapy, whereas IDH wild-type gliomas usually have a poorer prognosis and show resistance to such treatments. Therefore, precise prediction of IDH status can direct personalized treatment strategies. Similarly, accurately predicting 1p19q co-deletion status provides crucial information for treatment planning.

Despite promising results in using VASARI MRI features and machine learning to predict glioma molecular markers, this study has limitations. It explored only three machine learning models, and other models or combinations might enhance predictive accuracy. Furthermore, while this study focused on VASARI features, other potentially predictive elements like imaging histology features and ADC values were not included in our analysis.

In conclusion, this research demonstrates the potential of integrating VASARI MRI features with machine learning to predict glioma molecular markers, enabling more precise and individualized predictions for glioma patients. Such prognostic capabilities allow medical professionals to make informed and accurate treatment decisions, thereby improving patient outcomes. The findings are foundational for ongoing research in this field, with the potential to refine and expand this methodology to predict additional glioma markers, such as MGMT promoter methylation status, TERT promoter mutations, and TP53 mutations. The merging of radiomics with machine learning is poised to create even more personalized and precise prognostic tools for managing glioma patients.

Acknowledgements

This work was supported by Construction of AI Database and Platform for Medical Imaging of CNS Diseases in Xinjiang (2023TSYCLJ0027).

Disclosure of conflict of interest

None.

Address correspondence to: Yunling Wang, Imaging Centre, The First Affiliated Hospital of Xinjiang Medical University, No. 137 Liyushan South Road, Urumqi 830054, Xinjiang, China. Tel: +86-0991-4362658; E-mail: doctorwangyunling@163.com

References

[1] Guo X, Sui R and Piao H. Exosomes-mediated crosstalk between glioma and immune cells in the tumor microenvironment. CNS Neurosci Ther 2023; 29: 2074-2085.

[2] Xu S, Tang L, Li X, Fan F and Liu Z. Immunotherapy for glioma: current management and future application. Cancer Lett 2020; 476: 1-12.

[3] Yang K, Wu Z, Zhang H, Zhang N, Wu W, Wang Z, Dai Z, Zhang X, Zhang L, Peng Y, Ye W, Zeng W, Liu Z and Cheng Q. Glioma targeted therapy: insight into future of molecular approaches. Mol Cancer 2022; 21: 39.

[4] Louis DN, Perry A, Wesseling P, Brat DJ, Cree IA, Figarella-Branger D, Hawkins C, Ng HK, Pfister SM, Reifenberger G, Soffietti R, von Deimling A and Ellison DW. The 2021 WHO Classification of Tumors of the Central Nervous System: a summary. Neuro Oncol 2021; 23: 1231-1251.

[5] Gevaert O, Mitchell LA, Achrol AS, Xu J, Echegaray S, Steinberg GK, Cheshier SH, Napel S, Zaharchuk G and Plevritis SK. Glioblastoma multiforme: exploratory radiogenomic analysis by using quantitative image features. Radiology 2014; 273: 168-174.

[6] Gemini L, Tortora M, Giordano P, Prudente ME, Villa A, Vargas O, Giugliano MF, Somma F, Marchello G, Chiaramonte C, Gaetano M, Frio F, Di Giorgio E, D'Avino A, Tortora F, D'Agostino V and Negro A. Vasari scoring system in discerning between different degrees of glioma and IDH status prediction: a possible machine learning application? J Imaging 2023; 9: 75.

[7] Xue C, Zhou Q, Zhang B, Ke X, Zhang P, Liu X, Li S, Deng J and Zhou J. Vasari-based features nomogram to predict the tumor-infiltrating CD8+ T cell levels in glioblastoma. Acad Radiol 2024; 31: 2050-2060.

[8] You W, Mao Y, Jiao X, Wang D, Liu J, Lei P and Liao W. The combination of radiomics features and VASARI standard to predict glioma grade. Front Oncol 2023; 13: 1083216.

[9] Weller M, Wen PY, Chang SM, Dirven L, Lim M, Monje M and Reifenberger G. Glioma. Nat Rev Dis Primers 2024; 10: 33.

[10] Ammendola S, Broggi G and Barresi V. IDH-mutant diffuse gliomas: tips and tricks in the era of genomic tumor classification. Histol Histopathol 2023; 38: 739-753.

[11] Lin AP. Cystathionine: a spectroscopic biomarker for 1p/19q codeleted gliomas. Radiology 2023; 308: e232100.

[12] Hertler C, Felsberg J, Gramatzki D, Le Rhun E, Clarke J, Soffietti R, Wick W, Chinot O, Ducray F, Roth P, McDonald K, Hau P, Hottinger AF, Reijneveld J, Schnell O, Marosi C, Glantz M, Darlix A, Lombardi G, Krex D, Glas M, Reardon DA, van den Bent M, Lefranc F, Herrlinger U, Razis E, Carpentier AF, Phillips S, Rudà R, Wick A, Tabouret E, Meyronet D, Maurage CA, Rushing E, Rapkins R, Bumes E, Hegi M, Weyerbrock A, Aregawi D, Gonzalez-Gomez C, Pellerino A, Klein M, Preusser M, Bendszus M, Golfinopoulos V, von Deimling A, Gorlia T, Wen PY, Reifenberger G and Weller M. Long-term survival with IDH wildtype glioblastoma: first results from the ETERNITY Brain Tumor Funders' Collaborative Consortium (EORTC 1419). Eur J Cancer 2023; 189: 112913.

[13] Kinslow C, Siegelin MD, Iwamoto FM, Gallitto M, Neugut AI, Yu JB, Cheng SK and Wang TJC. MGMT promoter methylation in 1p19q-intact gliomas. Res Sq [Preprint] 2023; rs.3.rs-3393238.

[14] Mier-Garcia JF, Ospina-Santa S, Orozco-Mera J, Ma R and Plaha P. Supramaximal versus gross total resection in glioblastoma, IDH wild-type and astrocytoma, IDH-mutant, grade 4, effect on overall and progression free survival: systematic review and meta-analysis. J Neurooncol 2023; 164: 31-41.

[15] Mohile NA, Messersmith H, Gatson NT, Hottinger AF, Lassman A, Morton J, Ney D, Nghiemphu PL, Olar A, Olson J, Perry J, Portnow J, Schiff D, Shannon A, Shih HA, Strowd R, van den Bent M, Ziu M and Blakeley J. Therapy for diffuse astrocytic and oligodendroglial tumors in adults: ASCO-SNO guideline. J Clin Oncol 2022; 40: 403-426.

[16] Bai L, Jiang J and Zhou J. Assessment of Ki-67 expression levels in IDH-wildtype glioblastoma using logistic regression modelling of VASARI features. Neurosurg Rev 2023; 47: 20.

[17] Sacli-Bilmez B, Firat Z, Topcuoglu OM, Yaltirik K, Ture U and Ozturk-Isik E. Identifying overall survival in 98 glioblastomas using VASARI features at 3T. Clin Imaging 2023; 93: 86-92.

[18] Verduin M, Primakov S, Compter I, Woodruff HC, van Kuijk SMJ, Ramaekers BLT, te Dorsthorst M, Revenich EGM, ter Laan M, Pegge SAH, Meijer FJA, Beckervordersandforth J, Speel EJ, Kusters B, de Leng WWJ, Anten MM, Broen MPG, Ackermans L, Schijns OEMG, Teernstra O, Hovinga K, Vooijs MA, Tjan-Heijnen VCG, Eekers DBP, Postma AA, Lambin P and Hoeben A. Prognostic and predictive value of integrated qualitative and quantitative magnetic resonance imaging analysis in glioblastoma. Cancers (Basel) 2021; 13: 722.

[19] Zhang G, Tai P, Fang J, Chen A, Chen X and Cao K. Molecular subtypes based on centrosome-related genes can predict prognosis and therapeutic responsiveness in patients with low-grade gliomas. Front Oncol 2023; 13: 1157115.

[20] Park YW, Han K, Ahn SS, Bae S, Choi YS, Chang JH, Kim SH, Kang SG and Lee SK. Prediction of IDH1-mutation and 1p/19q-codeletion status using preoperative MR imaging phenotypes in lower grade gliomas. AJNR Am J Neuroradiol 2018; 39: 37-42.

[21] Setyawan NH, Choridah L, Nugroho HA, Malueka RG and Dwianingsih EK. Beyond invasive biopsies: using VASARI MRI features to predict grade and molecular parameters in gliomas. Cancer Imaging 2024; 24: 3.

[22] Sun C, Fan L, Wang W, Wang W, Liu L, Duan W, Pei D, Zhan Y, Zhao H, Sun T, Liu Z, Hong X, Wang X, Guo Y, Li W, Cheng J, Li Z, Liu X, Zhang Z and Yan J. Radiomics and qualitative features from multiparametric MRI predict molecular subtypes in patients with lower-grade glioma. Front Oncol 2022; 11: 756828.

[23] Zeng S, Ma H, Xie D, Huang Y, Wang M, Zeng W, Zhu N, Ma Z, Yang Z, Chu J and Zhao J. Quantitative susceptibility mapping evaluation of glioma. Eur Radiol 2023; 33: 6636-6647.

[24] Han Q, Lu Y, Wang D, Li X, Ruan Z, Mei N, Ji X, Geng D and Yin B. Glioblastomas with and without peritumoral fluid-attenuated inversion recovery (FLAIR) hyperintensity present morphological and microstructural differences on conventional MR images. Eur Radiol 2023; 33: 9139-9151.